A wall model for LES accounting for radiation effects

Yufang Zhang, Ronan Vicquelin, Olivier Gicquel, J Taine

A wall model for LES accounting for radiation effects

Y. F. Zhang[a,b], R. Vicquelin[a,b,*], O. Gicquel[a,b], J. Taine[a,b]

[a] *CNRS, UPR 288 Laboratoire d'Energétique Moléculaire et Macroscopique, Combustion (EM2C), Grande Voie des Vignes, 92295 Châtenay-Malabry, France.*

[b] *Ecole Centrale Paris, Grande Voie des Vignes, 92295 Châtenay-Malabry, France.*

Abstract

In several conditions, radiation can modify the temperature law in turbulent boundary layers. In order to predict such an effect and the corresponding change in conductive heat flux at the wall, a new wall model for large-eddy simulation (LES) is proposed. The wall model describes the inner boundary layer which cannot be resolved by the LES. The radiative power source term is calculated from an analytical expression of the intensity field within the inner layer. In the outer layer, wall stress and conductive heat flux predicted by the wall model are fed back to the large-eddy simulation which is coupled to a reciprocal Monte-Carlo method to account for radiation.

Several mixing-length models and turbulent Prandtl number formula are investigated. Then, the level of accuracy of the discretized radiation analytical model is investigated. Finally, fully coupled results are compared with Direct Numerical Simulation/Monte-Carlo results of turbulent channel flows at different Reynolds number, wall temperature and pressure conditions. The proposed wall model greatly improves the accuracy of the predicted temperature profiles and wall conductive heat fluxes compared to approaches without radiation accounted for in the inner layer.

Keywords: Wall model, LES, radiation, temperature, channel flow

*Corresponding author. Tel.: +33 1 41 13 10 90; Fax: +33 1 47 02 80 35.
Email address: ronan.vicquelin@ecp.fr (R. Vicquelin)

Roman Symbols

c_p	Thermal capacity at constant pressure [J·kg^{-1}·K^{-1}].
e	Optical thickness [-].
h	Enthalpy per unit mass [J·kg^{-1}].
I	Radiative intensity [W· m^{-2}· sr^{-1}].
L	Length [m].
p	Pressure [Pa].
Pr	Prandtl number [-].
P	Power per unit volume [W·m^{-3}].
q	Heat flux [W·m^{-2}].
Re	Reynolds number [-].
S_i	Momentum source term [N·m^{-3}].
t	Time [s].
T	Temperature [K].
u	Streamwise velocity component [m·s^{-1}].
u_i, u_j	Velocity vector [m·s^{-1}].
X, Y, Z	Cartesian coordinates [m].
x_i	Coordinate vector (tensorial) [m].
y	Distance to a wall [m].

Greek Symbols

δ	Channel half-width [m].
δ_{ij}	Kronecker delta operator [-].
κ	Spectral absorption coefficient [m^{-1}].
λ	Thermal conductivity [W·K^{-1}·m^{-1}].
ρ	Gas mass density [kg·m^{-3}].
τ_{ij}	Viscous shear stress tensor [N·m^{-2}].
Ω	Solid angle [sr].
ν	Radiation wave number [cm^{-1}] or kinematic viscosity [m^2/s].
θ	Polar angle [sr].
μ	Dynamic viscosity [kg·s^{-1}·m^{-1}] or cosine of polar angle [-].

Superscript

$\overline{\cdot}$	Filtered quantities.
$\widetilde{\cdot}$	Mass-weighted filtered quantities.
$''$	Mass-weighted fluctuating quantities.
SGS	Subgrid-scale quantities.
a	Absorbed quantities.
e	Emitted quantities.
0	Equilibrium quantities.
+	Wall-scaled quantities or quantity in positive y direction.
−	Quantities in negative y direction.

Subscript

b	Bulk quantities.
c , h	Refer to the cold wall, respectively to the hot wall.
cd	Conductive quantities.
R	Radiative quantities.
t	Turbulent Quantities.
w	Wall quantities.
y_w	Quantities at position $y = y_w$ of the 1D model.
τ	Friction quantities.
ν	Spectral quantities.
0	Quantities at position $y = 0$ of the 1D model.

Brackets

$\langle\cdot\rangle$	Reynolds averaged quantity in the 1D model.
$\{\cdot\}$	Favre averaged quantity in the 1D model.

Abbrevation

DNS	Direct Numerical Simulation.
LES	Large Eddy Simulation.
RANS	Reynolds-Averaged Numerical Simulations
OERM	Optimized Emission Reciprocity Method
TLM	Two-Layer Model
SGS	Sub-Grid Scale
rms	root mean square

1. Introduction

Fully resolved Large Eddy Simulation (LES) of the inner layer of a wall-bounded turbulent flow requires highly resolved grids since the integral length scale becomes of the same order of magnitude as viscous scales in the close vicinity of the wall. The computational cost is then proportional to $Re^{2.4}$ [1]. Hence, fully resolved LES is impracticable for wall-bounded flows at high Reynolds number, encountered in most of engineering applications, due to the prohibitive cost. Several kinds of approaches are commonly used in order to alleviate these difficulties: A wall model prescribes the correct wall shear stress to the LES that is too poorly resolved close to the wall to estimate it accurately.

In hybrid RANS/LES, the simulation is switched from RANS in the inner layer to LES in the outer layer by the modification of the length scales [2, 3] or the use of a blending function [4, 5] in the turbulent transport model. In other wall models for LES, the wall stress is estimated by using an algebraic wall function or by locally solving a simplified RANS equation. These approaches correspond to equilibrium-stress model and Two-Layer Model (TLM), respectively.

The equilibrium-stress model has been firstly proposed by Deardroff [6]. It has then been successfully applied to turbulent channel flows and annuli flows [7]. However, this model is restricted to simple flows, since it implies the existence of a logarithmic layer. In order to widen its use to more complex flows, the original equilibrium model has been modified by considering

inclination of the elongated structure in near wall region [8], pressure gradient [9, 10], buoyancy [11] or chemistry [12].

In two-layer models, turbulent boundary layer equations are resolved on a local embedded grid [13]. This approach has been extensively applied and assessed in different configurations [14, 15, 16]. Moreover, since all wall modeled LES unavoidably suffers from the numerical and sub-grid error at the first grid point close to a wall [14, 17], an effective strategy has recently been proposed by Kawai et al. [18] to increase the accuracy of the information transmitted from LES in the outer layer to the inner thin turbulent boundary layer equations.

A more detailed description of wall models for velocity is given in Refs. [19, 1, 14]. In order to deal with turbulent heat transfer and predict wall heat fluxes accurately, these wall models have to be extended to describe the thermal boundary layer as in [20, 21]. To the best of our knowledge, no wall model for LES has accounted for radiation effects, although radiation strongly modifies the temperature field in many applications, particularly in combustion processes at high pressure [22, 23, 24]. It has been recently shown [25] in coupled DNS-Monte Carlo simulations that radiation can significantly influence the temperature wall-law and the corresponding wall conductive heat flux. The temperature law is very different from the usual logarithmic law for strong radiation effects and has been observed to differ significantly under different radiative conditions. It is therefore unrealistic to hope for a general algebraic wall-law to account for these effects and a two-layer approach is then chosen. Besides, in order to predict the radiative field outside of the inner boundary layer, a reciprocal Monte-Carlo method is considered. The method is accurate and can be applied to complex geometries so that the proposed wall-model and its coupling with LES and the Monte-Carlo method remain general.

The objective of this study is to account for radiation effects in the inner layer wall model to accurately predict wall stress and heat flux. Here, a two-layer model is retained where, in the outer layer, LES is coupled to a radiation Monte Carlo method as in Ref. [25]. Coupled DNS-Monte Carlo results of Ref. [25] are considered to validate the proposed LES wall model. The fluid and radiation models in both layers are detailed in Sec. 2, followed by a description of coupling between the inner and outer layers. Separate validations of the different model components are presented in Sec. 3. Finally, in Sec. 4, fully coupled results assess the model accuracy.

2. Wall-modeled LES coupled to radiation

In all fluid simulations, LES is here carried out in the outer layer and the boundary inner layer is modeled by solving 1D balance equations. For radiation, a reciprocal Monte Carlo approach is implemented to estimate the radiative power at all LES grid points and an analytical radiative 1D model is developed for the inner layer. For both radiation and fluid models, a particular care is brought to the boundary conditions, especially between the inner and outer layers.

2.1. Fluid model

As shown in Fig. 1, an embedded grid is used in the inner layer. The inner layer model uses the velocity $\tilde{u}_{y_w}$ and temperature $\tilde{T}_{y_w}$ values computed by the LES model at a particular point characterized by the wall distance y_w. The wall stress τ_w and conductive heat flux q_w^{cd} computed by the inner layer model are then sent back to the LES solver.

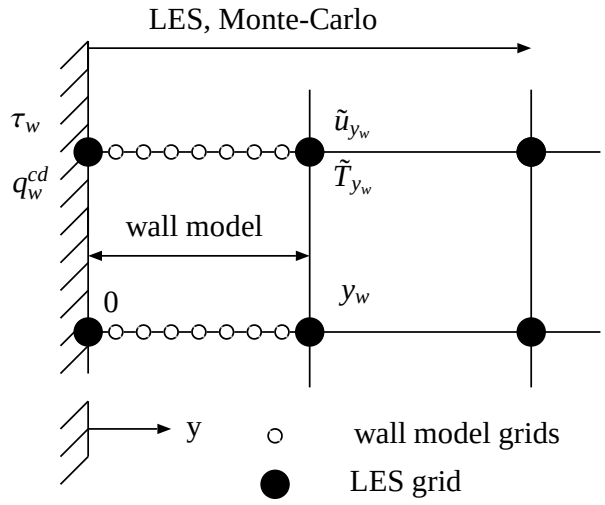

Figure 1: Scheme of wall model grids embedded within the LES grid. In this example, the wall distance y_w for the coupling point corresponds to the first LES grid point off the wall.

2.1.1. Inner layer fluid model

As explained in Ref. [1], filtered equations in the inner layer are similar to averaged Navier-Stokes equations. Then, treating the unresolved inner layer $[0, y_w]$ as a thin equilibrium boundary layer [15, 14] leads to the following equations

$$\frac{\mathrm{d}}{\mathrm{d}y}\left((\langle\mu\rangle + \langle\mu_t\rangle)\frac{\mathrm{d}\{u_{\|}\}}{\mathrm{d}y}\right) = 0; \quad \frac{\mathrm{d}}{\mathrm{d}y}\left(\langle c_p\rangle\left(\frac{\langle\mu\rangle}{\mathrm{Pr}} + \frac{\langle\mu_t\rangle}{\mathrm{Pr_t}}\right)\frac{\mathrm{d}\{T\}}{\mathrm{d}y}\right) + \langle P^R\rangle = 0, \tag{1}$$

where the angled brackets $\langle\cdot\rangle$ and curly brackets $\{\cdot\}$ denote Reynolds-averaged and Favre-averaged values respectively. $u_{\|}$ is the tangential velocity, parallel to the wall, and y is the distance to the wall. T is the temperature, P^R is the radiative power per unit volume. As in Ref. [25], μ, the dynamic viscosity, and c_p, the thermal capacity at constant pressure, are functions of temperature, while the molecular Prandtl number Pr is set to 0.71. μ_t and $\mathrm{Pr_t}$ are the turbulent viscosity and the turbulent Prandtl number, respectively. μ_t is computed using a mixing-length model [26, 14],

$$\langle\mu_t\rangle = \langle\rho\rangle\kappa y\sqrt{\langle\tau_w\rangle/\langle\rho\rangle}(1 - \exp(-y^+/A^+))^2\,, \tag{2}$$

where $\kappa = 0.4$ and $A^+ = 17$ are here chosen in order to retrieve the velocity logarithmic law in the low-Reynolds DNS cases that are considered for validation. $\langle\rho\rangle$ is the gas density and $\langle\tau_w\rangle$ the shear stress at the wall. The wall coordinate y^+ is defined as

$$y^+ = \frac{\langle\rho_w\rangle u_\tau y}{\langle\mu_w\rangle}, \qquad u_\tau = \sqrt{\frac{\langle\tau_w\rangle}{\langle\rho_w\rangle}}, \tag{3}$$

where gas properties at the wall, ρ_w and μ_w, are used. In order to take into account the non-uniformity of the gas properties, an alternative semi-local coordinate y^* [27] can also be used in

Eq. (2) instead of y^+, where local gas properties are considered

$$y^* = \frac{\langle\rho\rangle u_\tau^* y}{\langle\mu\rangle}, \qquad u_\tau^* = \sqrt{\frac{\langle\tau_w\rangle}{\langle\rho\rangle}}, \tag{4}$$

The mixing-length models based on wall coordinate y^+ and semi-local coordinate y^* will subsequently be referred as standard and semi-local mixing-length models, respectively.

Three models for the turbulent Prandtl number are considered in the following. First, a constant value $\mathrm{Pr_t} = 0.9$ which is a usual crude assumption in wall models. Secondly, in order to account for variation of $\mathrm{Pr_t}$ in the boundary layer, two different formula proposed in Ref. [28], both fitted from experimental data, are considered

$$\mathrm{Pr_t} = \frac{2.0}{\mathrm{Pr}\ (\langle\mu_t\rangle/\langle\mu\rangle)} + 0.85, \tag{5}$$

and

$$\mathrm{Pr_t} = \frac{1}{0.5882 + 0.228(\langle\mu_t\rangle/\langle\mu\rangle) - 0.0441(\langle\mu_t\rangle/\langle\mu\rangle)^2(1 - \exp(\frac{-5.165}{\langle\mu_t\rangle/\langle\mu\rangle}))}. \tag{6}$$

2.1.2. Outer layer LES

A low-Mach code, YALES2 [29, 30], is used for the Large Eddy Simulation (LES) of the main flow. The same numerical set-up as in Ref. [25] is retained: A 4th-order central difference finite-volume scheme with a 4th-order time integration scheme.

Under the low-Mach number approximation, the spatially filtered instantaneous mass, momentum and energy balance equations write

$$\frac{\partial\overline{\rho}}{\partial t} + \frac{\partial(\overline{\rho}\widetilde{u_i})}{\partial x_i} = 0, \tag{7}$$

$$\frac{\partial(\overline{\rho}\widetilde{u_i})}{\partial t} + \frac{\partial(\overline{\rho}\widetilde{u_i}\widetilde{u_j})}{\partial x_j} = \frac{\partial\tau_{ij}^{\mathrm{SGS}}}{\partial x_j} - \frac{\partial\overline{p}}{\partial x_i} + \frac{\partial\overline{\tau}_{ij}}{\partial x_j} + S_i, \tag{8}$$

$$\frac{\partial(\overline{\rho}\widetilde{\mathrm{h}})}{\partial t} + \frac{\partial(\overline{\rho}\widetilde{u_j}\widetilde{\mathrm{h}})}{\partial x_j} = -\frac{\partial q_j^{\mathrm{SGS}}}{\partial x_j} + \frac{\partial\overline{p}}{\partial t} - \frac{\partial\overline{q}_j^{cd}}{\partial x_j} + \overline{P}^R, \tag{9}$$

where p is the pressure, u_i the velocity components and $\overline{\cdot}$ and $\widetilde{\cdot}$ denote filtered and mass-weighted filtered quantities in the context of LES. The enthalpy per unit mass h is expressed as $\mathrm{h} = \Delta h_0 + \int_{T_0}^{T} c_p(T')\,dT'$, where c_p is the mixture thermal capacity at constant pressure, T_0 a reference temperature and Δh_0 the corresponding standard formation enthalpy. τ_{ij} and q_j^{cd} are the viscous shear stress tensor and the conductive heat flux vector respectively. S_i is a driving force source term to obtain the intended bulk Reynolds number in channel flow simulations.

Based on the Sub-Grid Scale (SGS) eddy-viscosity concept, the SGS stress tensor $\tau_{ij}^{\mathrm{SGS}} = -\overline{\rho}(\widetilde{u_i u_j} - \widetilde{u}_i\widetilde{u}_j)$ and the SGS heat flux $q_j^{\mathrm{SGS}} = \overline{\rho}(\widetilde{\mathrm{h}u_j} - \widetilde{\mathrm{h}}\widetilde{u}_j)$ are modeled as

$$\tau_{ij}^{\mathrm{SGS}} - \frac{1}{3}\delta_{ij}\tau_{kk}^{\mathrm{SGS}} = 2\overline{\rho}\nu^{\mathrm{SGS}}(\widetilde{S_{ij}} - \frac{1}{3}\delta_{ij}\widetilde{S}_{kk}), \tag{10}$$

$$q_j^{\mathrm{SGS}} = -\lambda^{\mathrm{SGS}}\frac{\partial\widetilde{T}}{\partial x_j}, \tag{11}$$

where $\widetilde{S}_{ij}$ is the filtered shear stress tensor. The Sigma model [31] is used for modeling the SGS kinematic viscosity ν^{SGS}. The SGS thermal conductivity λ^{SGS} is computed from the SGS Prandtl number $\mathrm{Pr}^{\mathrm{SGS}}$ which is set to 0.9

$$\lambda^{\mathrm{SGS}} = \frac{\overline{\rho}\,\overline{c_p}\nu^{\mathrm{SGS}}}{\mathrm{Pr}^{\mathrm{SGS}}}. \tag{12}$$

2.2. Radiation model

For the radiation field, a Monte-Carlo method is used to calculate the radiative power field in the outer layer, *i.e.* at all the LES grid points. For the inner layer, the radiation field is analytically obtained from a one-dimensional model that uses the intensity field obtained from the Monte Carlo approach as a boundary condition for the point with wall distance y_w, where information from the LES grid is fed back to the wall model.

2.2.1. Monte Carlo approach

The general organization of the radiation model, based on a reciprocal Monte Carlo approach, has been detailed by Tessé et al. [32]. The precise approach used here is the Optimized Emission-based Reciprocity Monte Carlo Method (OERM) [33], as in Ref. [25]. This method allows the convergence to be locally controlled while it overcomes the drawback of the original Emission-based Reciprocity Method [32] in the cold region and greatly increases the computational efficiency. This method also allows the spectral anisotropic radiation intensity field $I_\nu^-(y_w, \mu)$ at any point of abscissa y_w of the LES grid, required by the inner layer radiation model, to be determined, as detailed in Sec. 2.2.2 and Appendix.

2.2.2. Analytical radiation model in the inner layer

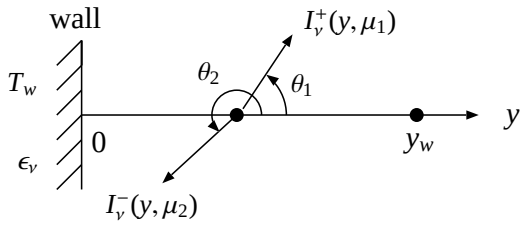

Figure 2: Definition of forward and backward intensities I_ν^+ and I_ν^- (μ_1 and μ_2 are the cosine of polar angle θ_1 and θ_2 respectively; $y = 0$ and $y = y_w$ are the two boundaries of the 1D model).

The one-dimensional configuration for radiation in the inner layer is shown in Fig. 2. The opaque wall is isothermal at temperature T_w and its emissivity ϵ_ν is assumed isotropic. At any point y of the inner layer, the radiative power per unit volume $P^R(y)$, difference between absorbed and emitted powers, writes

$$P^R(y) = P^a(y) - P^e(y) \tag{13}$$

$$P^e(y) = 4\pi \int_0^{+\infty} \kappa_\nu(y) I_\nu^\circ(y) d\nu \tag{14}$$

$$P^a(y) = \int_0^{+\infty} \kappa_\nu(y) \left[\int_{-1}^{0} I_\nu^-(y,\mu) 2\pi d\mu + \int_0^1 I_\nu^+(y,\mu) 2\pi d\mu \right] d\nu \tag{15}$$

where ν is the radiation wave number, μ is the cosine of the angle θ defined in Fig. 2, and $I^{\circ}_{\nu}(y)$ is the equilibrium spectral intensity at the temperature $T(y)$ associated with the current position y. The local spectral intensity in a positive y direction $I^{+}_{\nu}(y,\mu)$, associated with $\mu > 0$, and the spectral intensity in a negative direction $I^{-}_{\nu}(y,\mu)$, associated with $\mu < 0$ are given by

$$I^{+}_{\nu}(y,\mu) = \tau_{\nu 0y}(\mu) I^{+}_{\nu}(0) + \int_{0}^{y} \kappa_{\nu}(y') I^{\circ}_{\nu}(y') \tau_{\nu y'y}(\mu) \frac{dy'}{\mu} \quad \text{with: } y' < y;\ dy' > 0;\ \mu > 0, \tag{16}$$

$$I^{-}_{\nu}(y,\mu) = \tau_{\nu y_w y}(\mu) I^{-}_{\nu}(y_w,\mu) + \int_{y_w}^{y} \kappa_{\nu}(y') I^{\circ}_{\nu}(y') \tau_{\nu y'y}(\mu) \frac{dy'}{\mu} \quad \text{with: } y' > y;\ dy' < 0;\ \mu < 0, \tag{17}$$

where

$$I^{+}_{\nu}(0) = \epsilon_{\nu}\, I^{\circ}_{\nu}(T_w) \ - \ 2\,(1-\epsilon_{\nu}) \int_{-1}^{0} I^{-}_{\nu}(0,\mu)\, \mu d\mu, \tag{18}$$

and $\tau^{'}_{\nu y'y}$ is the directional spectral transmissivity between y' and y given by

$$\tau_{\nu y'y}(\mu) = \exp[-e_{\nu}(y',y)/\mu] \qquad \text{with :} \qquad e_{\nu}(y',y) = \int_{y'}^{y} \kappa_{\nu}(y'')\mathrm{d}y''. \tag{19}$$

Here $e_{\nu}(y',y)/\mu > 0$ is the spectral optical thickness between y' and y in the direction μ while κ_{ν} is the spectral absorption coefficient of the medium. Note that: i) dy' and μ in Eqs. (16) and (17), and $e_{\nu}(y',y)$ and μ in Eq. (19) are simultaneously positive or negative; ii) As the wall reflection is assumed diffuse, the intensity leaving a wall $I^{+}_{\nu}(0)$ is isotropic, whereas $I^{-}_{\nu}(y_w,\mu)$ the intensity entering the inner layer at abscissa y_w is anisotropic.

By introducing the exponential integral function, detailed in Ref. [34], *i.e.*

$$E_n(X) = \int_{0}^{1} \mu^{n-2} \exp(-X/\mu) d\mu \tag{20}$$

and the generalized incomplete function defined by

$$E_n(X,[\mu_j,\mu_{j+1}]) = \int_{\mu_j}^{\mu_{j+1}} \mu^{n-2} \exp(-X/\mu) d\mu, \tag{21}$$

a discretized expression of the radiative power $P^{R}(y)$ is simply given by

$$\begin{aligned} P^{R}(y) \approx\ & 2\pi \int_{0}^{+\infty} \kappa_{\nu}(y) \left\{ \sum_{j=1}^{N_{\mu}} E_2(e_{\nu}(y,y_w),[\mu_j,\mu_{j+1}])\, \overline{I}^{\,-}_{\nu}(y_w,[\mu_j,\mu_{j+1}]) \right\} d\nu \\ & + 2\pi \int_{0}^{+\infty} \kappa_{\nu}(y)\ E_2(e_{\nu}(0,y))\ I^{+}_{\nu}(0)\ d\nu \\ & + 2\pi \int_{0}^{+\infty} \kappa_{\nu}(y) \left\{ \int_{0}^{y_w} \kappa_{\nu}(y') I^{\circ}_{\nu}(y')\ E_1(e_{\nu}(y',y))\, dy' \right\} d\nu, \\ & - 4\pi \int_{0}^{+\infty} \kappa_{\nu}(y)\ I^{\circ}_{\nu}(y)\ d\nu. \end{aligned} \tag{22}$$

where N_μ is the number of angular sectors $[\mu_j, \mu_{j+1}]$ used to discretize the 2π steradians associated with the incoming intensity at a point y_w. $\overline{I}_\nu^-(y_w, [\mu_j, \mu_{j+1}])$ is the average value of $I_\nu^-(y_w, \mu)$ over the range $[\mu_j, \mu_{j+1}]$ [1].

The mean anisotropic spectral incoming intensity field $\overline{I}_\nu^-(y_w, [\mu_j, \mu_{j+1}])$ at any grid point y_w is determined by the Monte Carlo method, as detailed in Appendix.

In this analytical radiation model in the boundary inner layer, the radiative power $P^R(x)$ is a function of the temperature field within the fluid inner layer model given by Eq. (1). It is then worth noticing that the effects of turbulence fluctuations on the radiative power are not accounted for within the inner layer only. In fact, these effects can indeed be neglected in channel flows with non-reacting gases where fluctuations of temperature remain moderate, as shown by Ref. [22] and by post-processing of DNS results in Ref. [25] .

2.3. Coupling of inner and outer layers radiation and turbulence models

The purpose of wall-modeled LES is to overcome the under-resolution of the boundary inner layer, which leads to erroneous estimations of wall temperature and velocity gradients. For each LES grid point on the wall and each time step, the set of equations (1) combined with the analytical radiation model is solved with an iterative procedure and provides an accurate estimation of the wall stress τ_w and wall conductive heat flux q_w^{cd}. The procedure used to couple LES, Monte-Carlo model and the radiation and turbulence wall models is schematized in Fig. 3.

For each grid point on the wall, LES provides velocity u_{y_w} and temperature T_{y_w} at a distance y_w from the wall to the 1D turbulence model. It also provides the resolved temperature field T_{LES} to the Monte-Carlo method.

The Monte-Carlo method calculates both the radiative power P^R_{MC}, source term of the energy balance equation in LES, and the incoming intensities $\overline{I}_\nu^-(y_w, [\mu_j, \mu_{j+1}])$ required by the 1D radiation model.

Note that in the Monte Carlo method, when a ray enters the inner layer, the 1D-model temperature field from the previous iteration is used to determine the exchanged energy between the point initiating the ray and the inner layer. The accuracy of the results is then improved when compared to results associated only with the LES temperature field (much coarser in the near wall region).

Finally, the effect of delayed information between LES and both the wall model and radiation solver is here not investigated. Therefore, the coupling among LES, the Monte-Carlo method and the 1D wall model is carried out for each iteration of the LES solver. During the iterative procedure of the wall model between the 1D equations for the fluid fields and the 1D radiation model, the incoming intensity $\overline{I}_\nu^-(y_w, [\mu_j, \mu_{j+1}])$ specified by the Monte-Carlo method is fixed.

3. Separate validation of the turbulence and radiation wall model components

The previously described 1D turbulence wall model is *a priori* validated against DNS data from Ref. [25] accounting or not for radiation. This *a priori* study consists in comparing 1D profiles of averaged quantities predicted by the wall-model while taking some information from DNS cases.

[1] If $I_\nu^-(y_w, \mu)$ were isotropic the first term of the second member of Eq. (22) would be similar to the classical result of the second one.

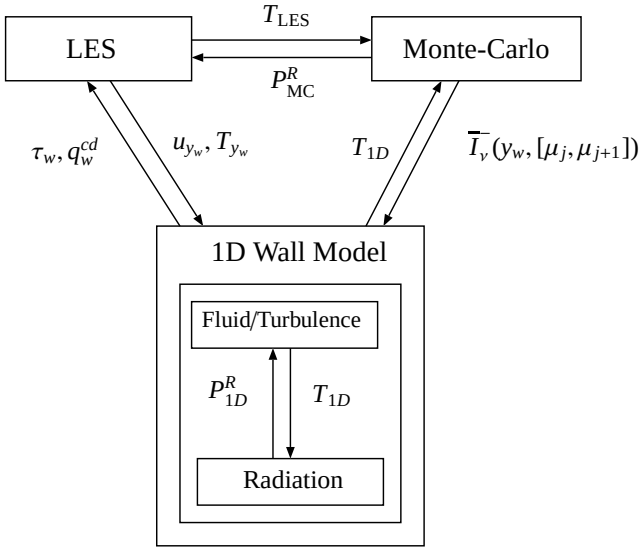

Figure 3: Scheme of coupling between LES, the Monte-Carlo method and the 1D wall models located at each point of the walls. T_{1D} and P^R_{1D} are the inner layer temperature and radiative power fields on the embedded grids.

DNS cases from Ref. [25] that are retained in this study are defined in Table 1. For cases A, B, C and D, the temperature of the two walls $T_{\text{w,h}}$ and $T_{\text{w,c}}$ are different, as shown in Fig. 4, and radiation is not accounted for. For cases A, B and C, the corresponding cases with radiation are named A_RAD, B_RAD and C_RAD respectively and opaque wall emissivities are set to 0.8. Two different cases at one atmosphere, named D_RAD03 and D_RAD08, are considered for case D with wall emissivities of 0.3 and 0.8 respectively. The gas radiative properties are modeled by using the CK model [35] for atmospheric pressure cases and its weak absorption limit for cases at 40 atm.

The domain is defined in Fig. 4 with : $\delta = 0.1m$, $L_X = 2\pi\delta$, $L_Y = 2\delta$, $L_Z = \pi\delta$. A non-reacting CO_2-H_2O-N_2 gas mixture is considered and the molar fractions of CO_2, H_2O and N_2 are set to 0.116, 0.155 and 0.729 to mimic combustion exhaust gases. Similarly to Ref. [25], the dynamic viscosity μ and thermal capacity c_p are computed as functions of temperature from the CHEMKIN package [36, 37] for the chosen mixture composition. The thermal conductivity λ is computed from the Prandtl number Pr= 0.71.

In the following sections, different wall-model components are separately validated.

3.1. Validation of the turbulence wall model without radiation

An integration of Eq. (1), in which the wall friction stress and wall heat flux results of DNS are imposed as boundary conditions, leads to velocity and temperature profiles in the near wall region. Since the proposed mixing-length model is only valid in the inner layer, only results within the near wall region (0, 0.2δ) are presented. The corresponding y^+ values at $y = 0.2\delta$ in wall coordinate are given in Tab. 2 for the different studied cases.

Velocity profile of case B that presents the most important wall temperature and gas properties variations is shown in Fig. 5. The velocity profile is under-predicted by the wall model based on standard mixing-length model, Eq. (3). The semi-local model, Eq. (4), enables to correct this

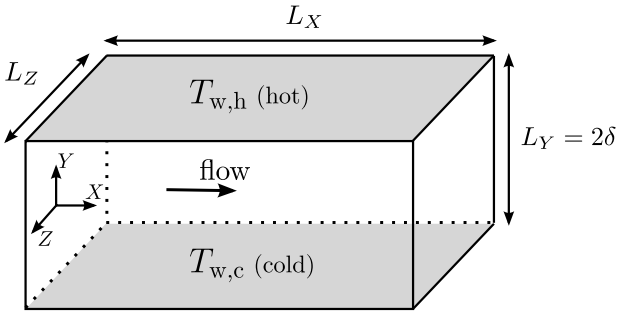

Figure 4: Computational domain of channel flow cases. X, Y and Z are the streamwise, wall-normal and spanwise directions. L_X, L_Y and L_Z are the dimensions of the channel case in each direction. δ is the channel half-width. The lower wall (resp. upper wall) is at temperature $T_{w,c}$ (resp. $T_{w,h}$; $T_{w,h} \geq T_{w,c}$). Periodic boundary conditions are applied along X and Z.

	$\mathrm{Re_b}$	Re_{D_h}	$T_{w,c}$ [K]	$T_{w,h}$ [K]	p [atm]
A	5850	23400	950	1150	40.0
B			950	2050	40.0
C	11750	47000	950	1150	40.0
D	5850	23400	950	1150	1.0

Table 1: Channel flow parameters: Bulk Reynolds number $\mathrm{Re_b}$, Reynolds number based on the hydraulic diameter $D_h = 4\delta$, wall temperatures and pressure. Cases without radiation A, B, C and D correspond to cases C1, C3, C4 and C2 in Ref. [25] respectively, and radiative cases A_RAD, B_RAD, C_RAD, D_RAD03 and D_RAD08 to cases C1R1, C3R1, C4R1, C2R2 and C2R1 respectively.

	A	A_RAD	B	B_RAD	C	C_RAD	D	D_RAD03	D_RAD08
Cold side	77.3	78.2	115.7	133.6	143.8	144.6	77.3	77.3	77.3
Hot side	61.1	66.7	45.9	52.1	111.4	113.4	61.0	61.3	61.4

Table 2: Wall normal distance y^+ in wall units corresponding to 0.2δ on both sides in each case.

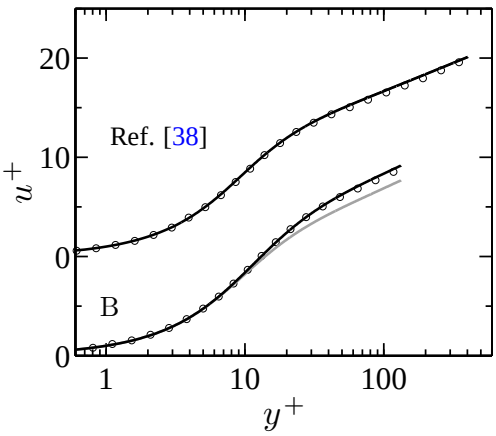

Figure 5: Mean velocity profile in wall units, *i.e.* $\{u\}/u_\tau$, of case B (only the cold side) and Ref. [38] (circles: DNS reference data; black line: Semi-local mixing-length model; gray line: Standard wall mixing-length model). For the sake of clarity, curves of the different cases are translated.

effect. When temperature variations are negligible, both models are identical and perform accurately as shown in Fig. 5 for the DNS case from Ref. [38] characterized by constant temperature and a larger Reynolds number.

Regarding the temperature profile, the two mixing-length models and the three models of turbulent Prandtl number defined in Sec. 2.1.1 are investigated in Fig. 6. Best results are obtained using the semi-local mixing-length model and Eq. (6) for the turbulent Prandtl number.

These modeling conditions are henceforth retained. Velocity and temperature profiles for cases A and C are shown in Fig. 7. Very good agreement with DNS data is observed.

3.2. Validation of the turbulence wall model with prescribed radiative power field

In this validation case, the reference radiative power issued from the radiation Monte Carlo method coupled to DNS is also used in addition to the DNS wall friction stress and wall heat flux in Eq. (1).

Figure 8 shows that the complete wall model (semi-local mixing-length model, Eq. (6) for $\mathrm{Pr_t}$ and radiative power source term) accurately predicts the temperature field for the two near wall regions of the three cases A_RAD, B_RAD and C_RAD. Note that the results of wall models that do not account for radiative power source term strongly deviate from the DNS corresponding results, which indicates that in these three cases, radiation strongly modifies the mean temperature field within the inner layer.

3.3. Validation of the radiation wall model with prescribed temperature field

In order to validate the radiative analytical wall model, Eq. (22) is solved using the mean temperature profile obtained from DNS data in Ref. [25] and N_μ spectral anisotropic incoming intensity values issued from the reference cases post-processing as explained in Appendix. The influence of the number of angular sectors N_μ and of the wall distance y_w where anisotropic intensities are calculated is investigated. Results are shown in Fig. 9. The radiative power is accurately predicted with $N_\mu = 2$ at each value of y_w between 0.05δ and 0.2δ. $N_\mu = 2$ is therefore used in the following. Note that results associated with $N_\mu = 1$ are practically acceptable.

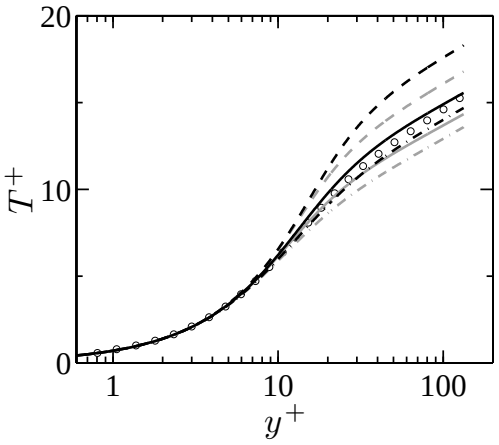

Figure 6: Mean temperature profile in wall units, *i.e.* $|\{T\} - T_w|/T_\tau$ with $T_\tau = |q_w^{cd}|/(\langle\rho_w\rangle c_{p_w} u_\tau)$, on the cold side of case B (circles: DNS data from Ref. [25]; black lines: Semi-local mixing-length model; gray lines: Standard mixing-length model; dashed-dotted line: Constant $\mathrm{Pr_t}$; dashed line: Eq. (5) for $\mathrm{Pr_t}$; plain line: Eq. (6) for $\mathrm{Pr_t}$).

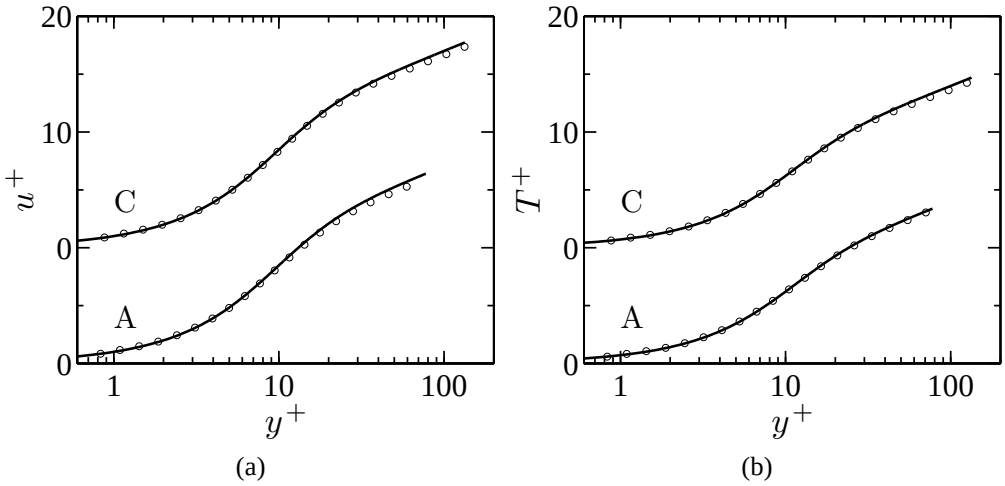

Figure 7: Mean velocity profile (a) and mean temperature profile (b) in wall units on the cold side of cases A and C (circles: DNS data from [25]; plain line: Semi-local mixing-length model + Eq. (6) for $\mathrm{Pr_t}$). For the sake of clarity, curves of the different cases are translated.

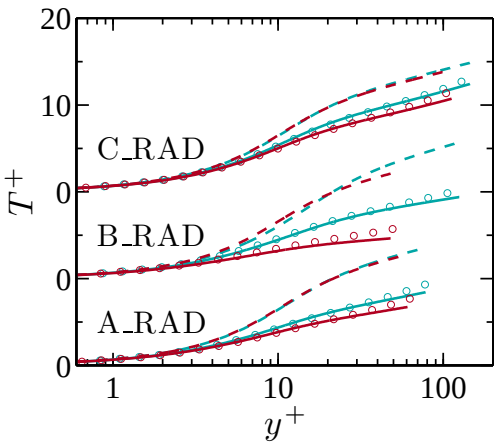

(a)

Figure 8: Mean temperature profile in wall units of cases A_RAD, B_RAD and C_RAD on the cold side (blue color) and hot side (red color) (circles: DNS data from [25]; dashed line: Wall model without radiative power source term; plain line: Wall model with radiative power source term).

4. Results of the turbulence and radiation wall models fully coupled with LES and Monte Carlo method

In this section, the turbulence and radiation wall models are fully coupled to LES and Monte Carlo models for the same cases A to D as in the previous section without prior knowledge from the reference DNS cases. For all these cases, the LES grid consists of $36 \times 36 \times 36$ points and the first off-wall point locates at $y^+ = 15$, while all the other grid spacings are uniform. The wall model, defined by Eqs. (1, 22), is resolved at each point on the wall on a local embedded grid (see Fig. 1). Given first guesses of the wall shear stress and wall heat flux, this set of equations is iteratively solved while ensuring grid convergence.

4.1. Cases without radiation

When coupling LES and wall models, numerical and sub-grid model errors at the first few points near the wall induce perturbations within the LES domain [14, 17], leading to the so-called "logarithmic law mismatch" [1]. The term "logarithmic law mismatch" specifically refers to cases where a logarithmic law is found for the velocity profile. A similar mismatch between the wall modeled LES and the reference results can also be observed for the temperature profile of the different cases studied here, where the temperature law is not logarithmic as soon as radiation is accounted for.

In order to reduce this error, Kawai et al.[18] have proposed to place the feed back point of the wall model, placed at the wall distance y_w, further away from the wall than the first off-wall LES grid point. Following this approach, different y_w positions are compared, *i.e.* y_w located at the first point, second and third off-wall points, denoted case Y1, Y2 and Y3 respectively. The corresponding embedded grids, which are stretched along the wall normal direction, contain 30, 60 and 100 points.

Figure 10 shows that, for case A, the case Y3 presents the best agreement for both u^+ and T^+ profiles as expected. This trend is retrieved for wall friction stress τ_w and conductive heat flux

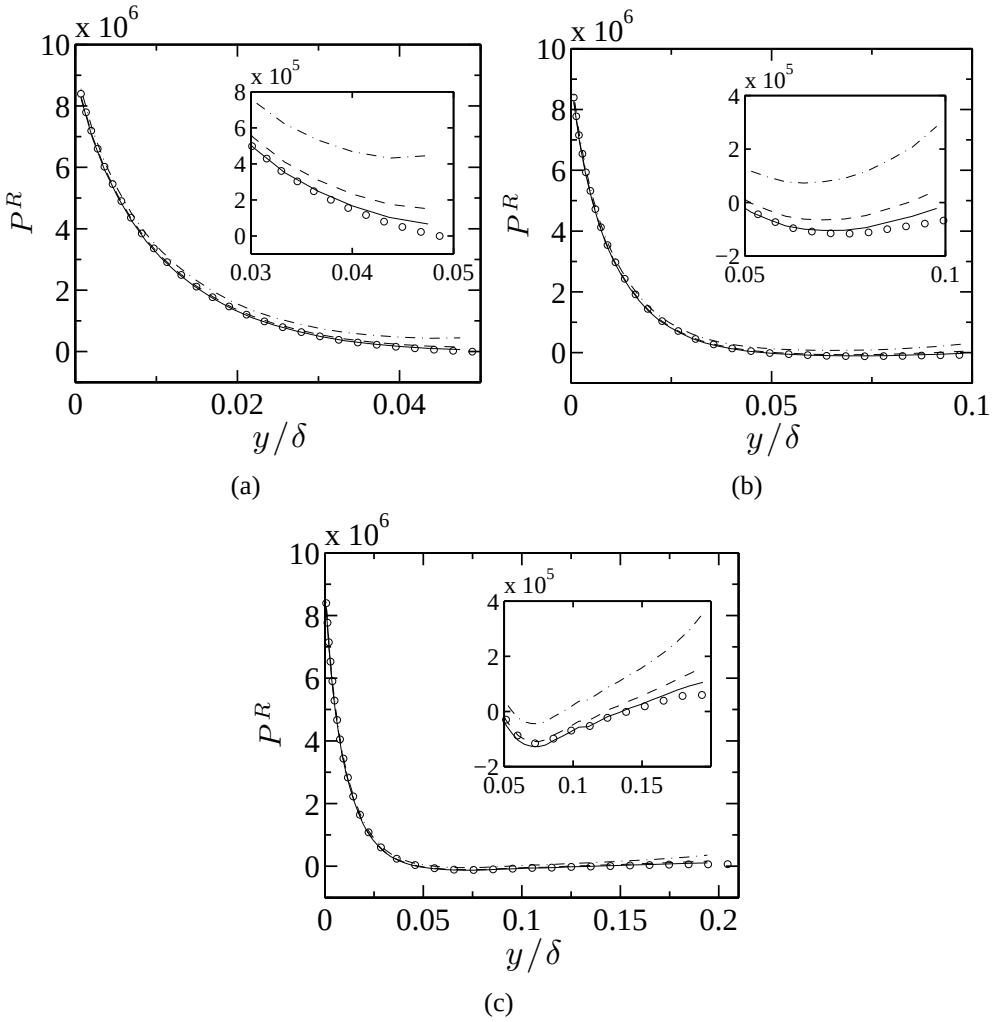

Figure 9: Radiative power in W.m^{-3} on the cold side of case B with $y_w = 0.05\delta$ (a), $y_w = 0.1\delta$ (b) and $y_w = 0.2\delta$ (c) (circles: DNS data from Ref. [25]; dashed-dotted line: $N_\mu = 1$; dashed line: $N_\mu = 2$; plain line: $N_\mu = 3$).

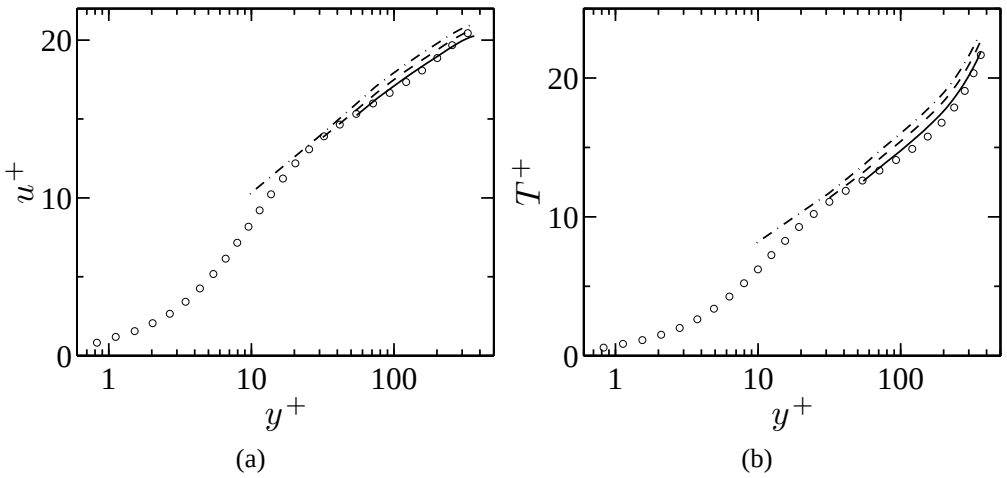

Figure 10: Mean velocity (a) and mean temperature (b) profile in wall units on the cold side of case A (circles: DNS data from [25]; dashed-dotted line: Y1; dashed line: Y2; plain line: Y3).

q_w^{cd} values shown in Tab. 3. The feed back point position does not affect the root mean square (rms) profiles of u, v, w and T (see Fig. 11). Henceforward, the third off-wall point is retained as a feed back point.

Results for cases B and C are presented in Fig. 12 and Tab. 3 demonstrating the relevance of this choice.

4.2. Cases involving radiation at high pressure

The finally proposed wall model based on semi-local mixing-length model, Eq. (6) for $\mathrm{Pr_t}$, the radiation analytical model described in Sec. 2.2.2 and using the third off-wall point for coupling (case Y3) will be denoted as "new" wall model. In order to demonstrate the accuracy of this model, it is compared to a "standard" wall model based on standard mixing-length model and constant turbulent Prandtl number, that does not account for radiation effects within the inner layer. Note that this "standard" model is also coupled at the third off-wall point and that radiation is treated with the Monte-Carlo method in the outer layer. Results without any wall model are also presented.

DNS results for profiles of u^+ and T^+ in cases A_RAD, B_RAD and C_RAD are compared in Fig. 13 to those predicted by wall-modeled LES with the "standard" and "new" approaches. The velocity field is similarly reproduced by both models whereas the "new" model shows a significant improvement of the predicted temperature profile. Values of τ_w and q_w^{cd} for the different cases are given in Tab. 4 where the same conclusion is retrieved. The wall radiative flux q_w^{R*}, without its passive wall-wall component that accounts for radiative energy exchanged between walls while considering the transmissivity of the fluid region, is also given for the case A_RAD only, showing a fair agreement between the value predicted by the proposed wall model and the one from DNS results.

4.3. Case involving radiation at 1 atm

Cases A to C correspond to optically thick media at 40 atm, in which the effects of radiation are important. Case D, considered in this paragraph and defined in Tab. 1, deals with media at

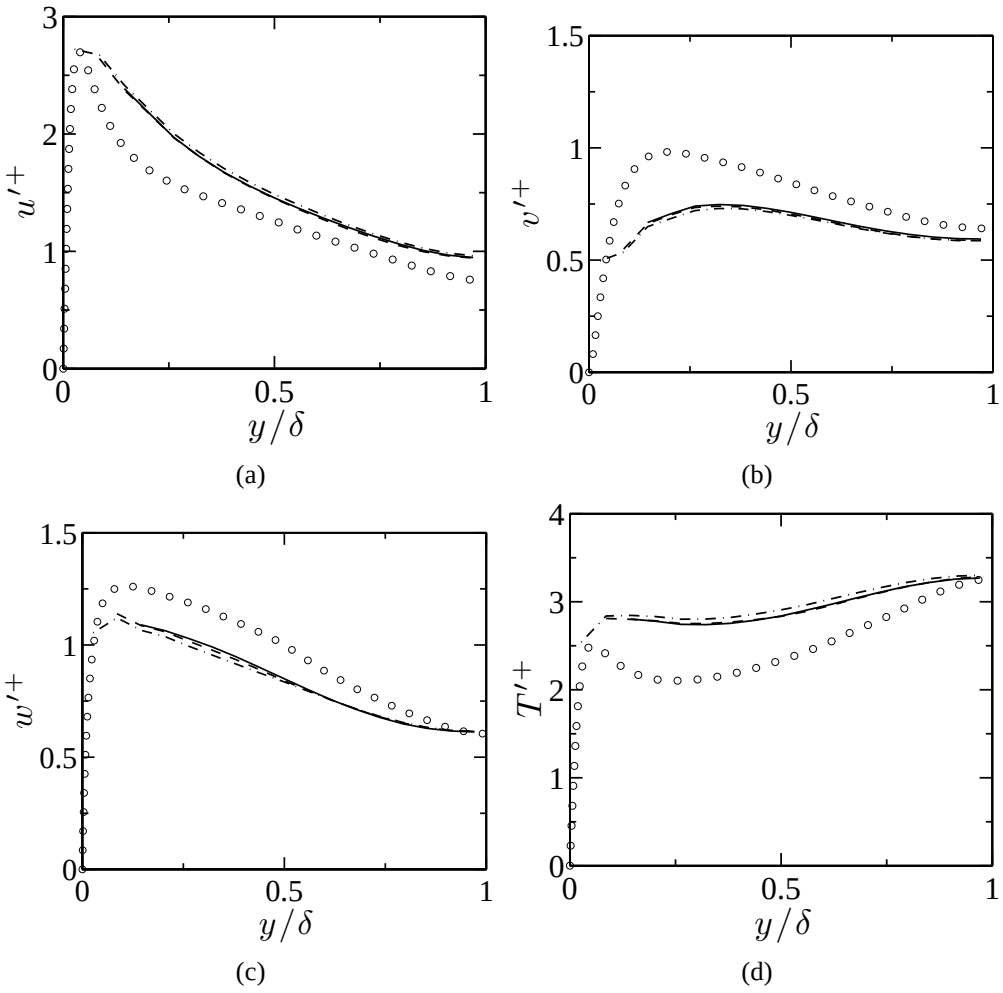

Figure 11: Rms of velocity components *u* (a), *v* (b), *w* (c) and temperature (d) in wall units on the cold side of case A (circles: DNS data from [25]; dashed-dotted line: Y1; dashed line: Y2; plain line: Y3).

		side	DNS	Y1	Y2	Y3
A	τ_w	cold	1.63E-3	1.50E-3	1.54E-3	1.60E-3
		hot	1.62E-3	1.55E-3	1.57E-3	1.61E-3
	q_w^{cd}	cold	875	813	837	873
		hot	875	813	834	870
B	τ_w	cold	3.69E-3	–	–	3.73E-3
		hot	3.57E-3	–	–	3.89E-3
	q_w^{cd}	cold	6510	–	–	6804
		hot	6510	–	–	6766
C	τ_w	cold	5.7E-3	–	–	5.4E-3
		hot	5.5E-3	–	–	5.4E-3
	q_w^{cd}	cold	1550	–	–	1502
		hot	1550	–	–	1498

Table 3: Comparison of mean wall shear stress τ_w and wall conductive heat flux q_w^{cd} for cases A, B and C between wall-modeled LES (Y1, Y2, Y3) and DNS results from Ref. [25]. For case A, Y1, Y2 and Y3 correspond to wall-normal distances of 0.05δ, 0.098δ and 0.156δ respectively.

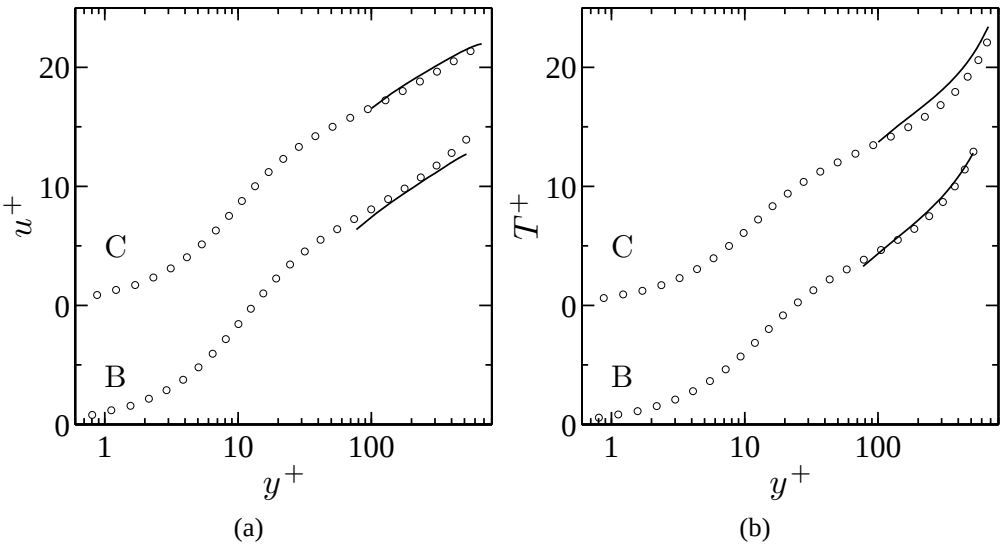

Figure 12: Mean velocity (a) and mean temperature (b) profile in wall units on the cold side of cases B and C (circles: DNS data from [25]; plain line: Y3). For the sake of clarity, curves of the different cases are translated.

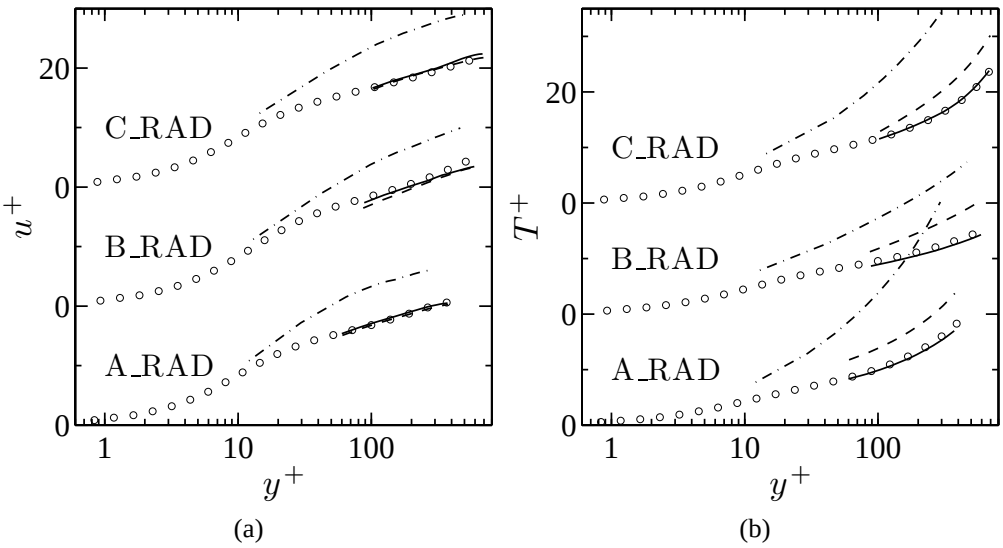

Figure 13: Mean velocity (a) and mean temperature (b) profile in wall units on the cold side of cases A_RAD, B_RAD and C_RAD (circles: DNS data from [25]; dashed-dotted line: No wall model; dashed line: Standard wall model; plain line: New wall model). For the sake of clarity, curves of the different cases are translated.

atmospheric pressure. LES of the two cases D_RAD03 and D_RAD08, with wall emissivities set to 0.3 and 0.8 respectively, with the "new" and "standard" wall models are compared with DNS data from Ref. [25].

Figure 14 (a) compares the u^+ profiles that are only shown on the cold side (similar on the hot side) and demonstrates that both models predict the correct result as in the high pressure cases. The same behavior is observed for the wall shear stress in Tab. 4.

Regarding the T^+ profiles (Figs. 14.b and 14.c) and wall conductive fluxes given in Tab. 4, the "new" model leads to the best agreement with DNS-Monte Carlo results compared to the "standard" model. However, since the radiation effects are weaker at 1 atm than at 40 atm, the difference between the results of the two wall-modeled LES are smaller than those at high pressure, especially on the cold side.

5. Conclusion

A wall model for LES has been proposed to take into account the effects of radiation within the turbulent boundary inner layer. The model follows a two-layer approach with an embedded grid for each point at the wall. It is composed of 1D equilibrium thin boundary layer equations that are solved on each embedded grid along with mixing-length and turbulent Prandtl models and an analytical expression of the radiative source term within the inner layer.

First results have shown that: i) A semi-local scaling of the mixing-length is necessary to account for the variations of gas properties, such as mass density and dynamic viscosity, within the inner layer; ii) A non-constant turbulent Prandtl number, here Eq. (6), gives better results; iii) In the studied cases, the mean incoming intensity at the outer boundary of the wall model has required the discretization of the corresponding solid angle into at least two angular sectors to accurately account for anisotropy; iv) The point where information is transmitted from LES

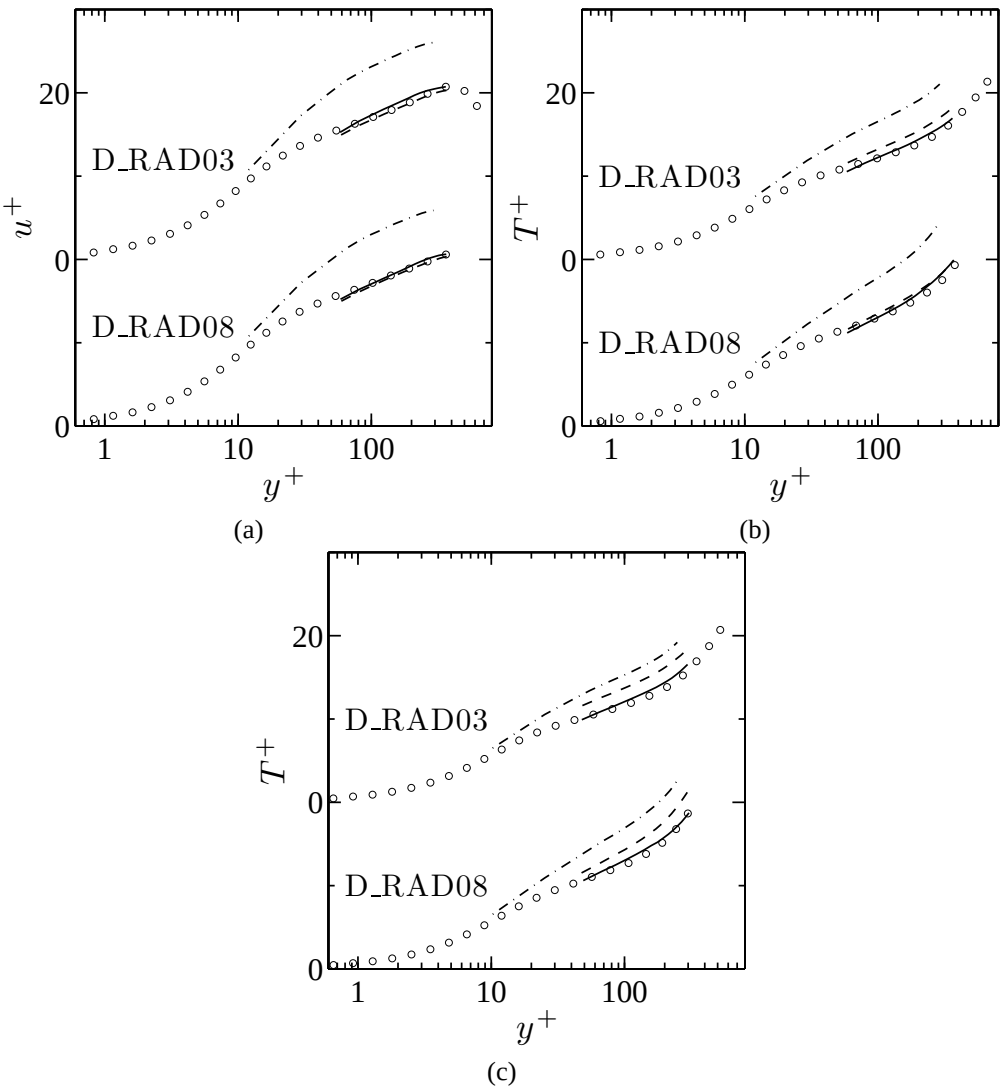

Figure 14: Mean velocity profile in wall units on the cold side (a), mean temperature profile in wall units on the cold side (b) and hot side (c) of cases D_RAD03 and D_RAD08 (circles: DNS data from [25]; dashed-dotted line: No wall model; dashed line: Standard wall model; plain line: New wall model). Curves of the different cases are translated.

to the wall model has been moved away from the wall while remaining in the validity range of the wall-model. Here, the third grid point off the wall has been used in order to decrease the mismatch in the obtained wall laws due to numerical and sub-grid errors in the wall vicinity.

The LES is coupled to a reciprocal Monte-Carlo method in such a way that it could be done in any configuration to tackle radiation and turbulent flows. Here, the combination of the proposed wall model and LES/Monte-Carlo method is compared to DNS/Monte-Carlo results on turbulent channel flows. Coupled results are compared to those obtained with a standard wall model which does not account for radiation effects within the inner layer. Note that this standard model with LES and Monte-Carlo simulations is already quite advanced to accurately predict wall heat transfer in the presence of radiation. Nonetheless, coupled results for high pressure cases show that the new wall-model greatly improves the accuracy of the predicted results compared to a standard wall model. The same trend is retrieved in atmospheric cases even though the magnitude of difference is smaller than the one at high pressure.

Finally, it has been shown that accounting for radiation effects within the modeled boundary inner layer is necessary in several conditions, especially in high pressure applications, as soon as the radiative energy transfer is strong enough to modify the temperature wall law. Deeper investigation is nonetheless still necessary to fully characterize when such effects can be expected and therefore when the proposed wall model should be applied.

Acknowledgments

We thank the China Scholarship Council (CSC) for granting a doctoral fellowship to the first author. This work was granted access to the HPC resources of [CCRT/CINES/IDRIS] under the allocations 2012-2b0164 and 2013-2b0164 made by GENCI (Grand Equipement National de Calcul Intensif). We are grateful to Dr. Philippe Riviere for providing the database of the Correlated-K model. We also acknowledge Dr. Vincent Moureau and the SUCCESS scientific group for providing the code YALES2 and support.

Appendix : Determination of the incoming intensity field for the wall model

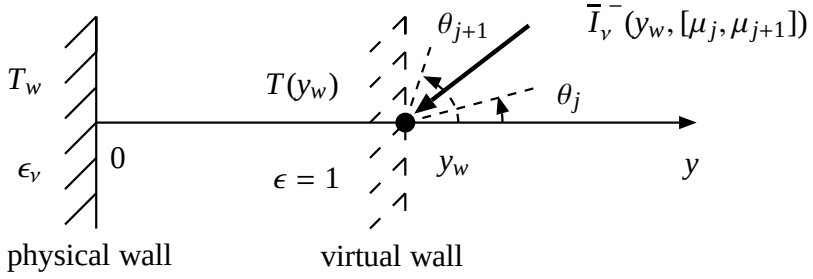

Figure 15: Scheme showing how the mean incoming intensity $\bar{I}_\nu^-(y_w,[\mu_j,\mu_{j+1}])$, boundary condition of the wall model, is computed from the reciprocal Monte-Carlo method by using a virtual wall. μ_j and μ_{j+1} correspond to the cosine of angles θ_j and θ_{j+1} respectively.

As described in Sec. 2.2.2, the proposed wall model requires mean anisotropic spectral incoming intensities $\bar{I}_\nu^-(y_w,[\mu_j,\mu_{j+1}])$ at a grid point y_w averaged over the solid angles corresponding

to the ranges $[\mu_j, \mu_{j+1}]$ as a boundary condition. The emission-based reciprocity Monte Carlo method defined in Ref. [25] is used in this paper. Consequently, the mean spectral intensities can easily be deduced from reciprocal emission phenomena issued from all the other cells of the system.

The precise used procedure described in Fig. 15 is the following: i) The grid point at wall distance y_w is assumed to be a virtual opaque wall of temperature $T(y_w)$ and of arbitrary wall emissivity $\epsilon = 1$; ii) For each range $[\mu_j, \mu_{j+1}]$, a large number of shots are emitted in the Monte Carlo method from this virtual wall in a randomly determined direction with the cosine of polar angle within the range $[\mu_j, \mu_{j+1}]$, and in any elementary spectral range $\Delta\nu$; iii) The reciprocity method allows $\Phi_{\Delta\nu}(y_w, [\mu_j, \mu_{j+1}])$, the contribution to the radiative flux at the virtual wall associated with both $[\mu_j, \mu_{j+1}]$ and $\Delta\nu$, to be determined; vi) The absorbed flux at the wall $\Phi^a_{\Delta\nu}(y_w, [\mu_j, \mu_{j+1}])$, and consequently the mean spectral absorbed intensity $\overline{I}^a_\nu(y_w, [\mu_j, \mu_{j+1}])$, associated with $[\mu_j, \mu_{j+1}]$ and $\Delta\nu$ are then calculated as

$$\Phi^a_{\Delta\nu}(y_w, [\mu_j, \mu_{j+1}]) = \Phi_{\Delta\nu}(y_w, [\mu_j, \mu_{j+1}]) + \Phi^e_{\Delta\nu}(y_w, [\mu_j, \mu_{j+1}]), \tag{23}$$

$$\overline{I}^a_\nu(y_w, [\mu_j, \mu_{j+1}]) = \frac{\Phi^a_{\Delta\nu}(y_w, [\mu_j, \mu_{j+1}])}{2\pi \int_{\mu_j}^{\mu_{j+1}} \mu \, d\mu \, \Delta\nu} = \frac{\Phi_{\Delta\nu}(y_w, [\mu_j, \mu_{j+1}])}{2\pi \int_{\mu_j}^{\mu_{j+1}} \mu \, d\mu \, \Delta\nu} + I^0_\nu(y_w); \tag{24}$$

v) The mean spectral incoming intensity $\overline{I}^-_\nu(y_w, [\mu_j, \mu_{j+1}])$ required by the wall model is then equal to $\overline{I}^a_\nu(y_w, [\mu_j, \mu_{j+1}])$, as the virtual wall absorptivity has been set to unity.

Reference

[1] U. Piomelli, Wall-layer models for large-eddy simulations, Prog. Aerosp. Sci. 44 (2008) 437–446.

[2] P. Spalart, W. Jou, M. Strelets, S. Allmaras, Comments of feasibility of les for wings, and on a hybrid RANS/LES approach, in: International Conference on DNS/LES, Aug. 4-8, 1997, Ruston, Louisiana.

[3] N. V. Nikitin, F. Nicoud, B. Wasistho, K. D. Squires, P. R. Spalart, An approach to wall modeling in large-eddy simulations, Phys. Fluids 12 (2000) 1629–1632.

[4] F. Hamba, A hybrid rans/les simulation of turbulent channel flow, Theor. Comp. Fluid Dyn. 16 (2003) 387–403.

[5] M. L. Shur, P. R. Spalart, M. K. Strelets, A. K. Travin, A hybrid RANS-LES approach with delayed-DES and wall-modelled LES capabilities, Int J. Heat Fluid Fl. 29 (2008) 1638–1649.

[6] J. W. Deardorff, A numerical study of three-dimensional turbulent channel flow at large reynolds numbers, J. Fluid Mech. 41 (1970) 453–480.

[7] U. Schumann, Subgrid scale model for finite difference simulations of turbulent flows in plane channels and annuli, J. Comput. Phys. 18 (1975) 376–404.

[8] U. Piomelli, J. Ferziger, P. Moin, J. Kim, New approximate boundary conditions for large eddy simulations of wall-bounded flows, Phys. Fluids A-Fluid 1 (1989) 1061–1068.

[9] M. Wang, LES with wall models for trailing edge aeroacoustics, Technical Report, Center for Turbulence Research, Stanford, CA, 1999.

[10] C. Duprat, G. Balarac, O. Metais, P. M. Congedo, O. Brugiere, A wall-layer model for large-eddy simulations of turbulent flows with/out pressure gradient, Phys. Fluids 23 (2011) 015101.

[11] C.-H. Moeng, A large-eddy-simulation model for the study of planetary boundary-layer turbulence, J. Atoms. Sci. 41 (1984) 2052–2062.

[12] O. Cabrit, F. Nicoud, Direct simulations for wall modeling of multicomponent reacting compressible turbulent flows, Phys. Fluids 21 (2009).

[13] E. Balaras, C. Benocci, U. Piomelli, Two-layer approximate boundary conditions for large-eddy simulations, AIAA J. 34 (1996) 1111–1119.

[14] W. Cabot, P. Moin, Approximate wall boundary conditions in the large-eddy simulation of high reynolds number flow, Flow Turbul. Combust. 63 (2000) 269–291.

[15] M. Wang, P. Moin, Dynamic wall modeling for large-eddy simulation of complex turbulent flows, Phys. Fluids 14 (2002) 2043–2051.

[16] A. Gungor, S. Menon, Direct simulation of subgrid turbulence in a high-*Re* wall-bounded flow., AIAA Paper 2006-3538 (2006).
[17] F. Nicoud, J. Baggett, P. Moin, W. Cabot, Large eddy simulation wall-modeling based on suboptimal control theory and linear stochastic estimation, Phys. Fluids 13 (2001) 2968–2984.
[18] S. Kawai, J. Larsson, Wall-modeling in large eddy simulation: Length scales, grid resolution, and accuracy, Phys. Fluids 24 (2012).
[19] U. Piomelli, E. Balaras, Wall-layer models for large-eddy simulations, Annu. Rev. Fluid Mech. 34 (2002) 349–374.
[20] Y. Benarafa, O. Clonia, F. Ducros, P. Sagaut, Temperature wall modelling for large-eddy simulation in a heated turbulent plane channel flow, Int J. Heat Mass Transfer 50 (2007) 4360–4370.
[21] S. L. Rani, C. E. Smith, A. C. Nix, Boundary-Layer Equation-Based Wall Model for Large-Eddy Simulation of Turbulent Flows with Wall Heat Transfer, Numer. Heat Tr. B-Fund. 55 (2009) 91–115.
[22] A. Gupta, M. F. Modest, D. C. Haworth, Large-Eddy Simulation of Turbulence-Radiation Interactions in a Turbulent Planar Channel Flow, J. Heat Trans.-T. ASME 131 (2009).
[23] A. Soufiani, P. Mignon, J. Taine, Radiation effects on turbulent heat transfer in channel flows of infrared active gases, in: Proceedings of the 1990 AIAA/ ASME thermophysics and heat transfer conference, HTD-137, ASME, pp. 141–148.
[24] S. Ghosh, R. Friedrich, M. Pfitzner, C. Stemmer, B. Cuenot, M. El Hafi, Effects of radiative heat transfer on the structure of turbulent supersonic channel flow, J. Fluid Mech. 677 (2011) 417–444.
[25] Y. F. Zhang, R. Vicquelin, O. Gicquel, J. Taine, Physical study of radiation effects on the boundary layer structure in a turbulent channel flow, Int J. Heat Mass Transfer 61 (2013) 654–666.
[26] W. Cabot, Near-wall models in large-eddy simulations of flow behind a backward-facing step, Technical Report, Center for Turbulence Research, Stanford, CA, 1996.
[27] P. Huang, G. Coleman, P. Bradshaw, Compressible turbulent channel flows: DNS results and modelling, J. Fluid Mech. 305 (1995) 185–218.
[28] W. M. Kays, Turbulent Prandtl number. Where are we?, J. Heat Trans.-T. ASME 116 (1994) 284–295.
[29] V. Moureau, P. Domingo, L. Vervisch, From Large-Eddy Simulation to Direct Numerical Simulation of a lean premixed swirl flame: Filtered laminar flame-PDF modeling, Combust. Flame 158 (2011) 1340–1357.
[30] V. Moureau, P. Domingo, L. Vervisch, Design of a massively parallel CFD code for complex geometries, Compt. Rendus. Mec. 339 (2011) 141–148.
[31] F. Nicoud, H. B. Toda, O. Cabrit, S. Bose, J. Lee, Using singular values to build a subgrid-scale model for large eddy simulations, Phys. Fluids 23 (2011) 085106.
[32] L. Tessé, F. Dupoirieux, B. Zamuner, J. Taine, Radiative transfer in real gases using reciprocal and forward Monte Carlo methods and a correlated-k approach, Int J. Heat Mass Transfer 45 (2002) 2797 – 2814.
[33] Y. F. Zhang, O. Gicquel, J. Taine, Optimized Emission-based Reciprocity Monte Carlo Method to speed up computation in complex systems, Int J. Heat Mass Transfer 55 (2012) 8172–8177.
[34] M. F. Modest, Radiative Heat Transfer, Academic Press, 2003.
[35] A. Soufiani, J. Taine, High temperature gas radiative property parameters of statistical narrow-band model for H_2O, CO_2 and CO, and correlated-K model for H_2O and CO_2, Int J. Heat Mass Transfer 40 (1997) 987 – 991.
[36] R. J. Kee, G. Dixon-lewis, J. Warnatz, M. E. Coltrin, J. A. Miller, A Fortran Computer Code Package For The Evaluation Of Gas-Phase, Multicomponent Transport Properties, Technical Report SAND89-8009, Sandia National Laboratories, 1986.
[37] R. J. Kee, F. M. Rupley, J. A. Miller, CHEMKIN-II: A Fortran Chemical Kinetics Package for the Analysis of Gas-Phase Chemical Kinetics, Technical Report SAND89-8009, Sandia National Laboratories, 1989.
[38] S. Hoyas, J. Jimenez, Scaling of the velocity fluctuations in turbulent channels up to $\mathrm{Re}_\tau = 2003$, Phys. Fluids 18 (2006) 011702.

		side	DNS	new model	standard model	no model
A_RAD	τ_w	cold	1.67E-3	1.64E-3	1.68E-3	1.0E-3
		hot	1.59E-3	1.63E-3	1.61E-3	1.09E-3
	q_w^{cd}	cold	1230	1270	918	443
		hot	960	1030	631	363
	$q_w^{R^*}$	cold	6970	6630	–	–
		hot	7240	7060	–	–
B_RAD	τ_w	cold	5.0E-3	4.8E-3	4.82E-3	3.1E-3
		hot	4.6E-3	4.6E-3	4.37E-3	3.1E-3
	q_w^{cd}	cold	16260	16041	10985	6583
		hot	8720	8911	3738	3303
C_RAD	τ_w	cold	5.7E-3	5.6E-3	5.71E-3	3.24E-3
		hot	5.5E-3	5.4E-3	5.37E-3	3.51E-3
	q_w^{cd}	cold	1650	1666	1288	660
		hot	1290	1358	925	569
D_RAD03	τ_w	cold	6.6E-3	6.3E-3	6.5E-3	4.0E-3
		hot	6.5E-3	6.3E-3	6.4E-3	4.4E-3
	q_w^{cd}	cold	1220	1180	1105	677
		hot	1100	1055	955	622
D_RAD08	τ_w	cold	6.6E-3	6.4E-3	6.6E-3	4.1E-3
		hot	6.5E-3	6.6E-3	6.3E-3	4.5E-3
	q_w^{cd}	cold	1070	1040	1018	773
		hot	930	926	821	750

Table 4: Comparison of mean wall shear stress τ_w, wall conductive heat flux q_w^{cd} and wall radiative flux $q_w^{R^*}$ between wall-modeled LES (new, standard and no wall model) and DNS results from Ref. [25] (the wall-wall radiative flux is not included in $q_w^{R^*}$).